Precise Model for Small-Body Thermal Radiation Pressure Acting on Spacecraft

Journal Item

A Precise Model for Small Body Thermal Radiation Pressure Acting on Spacecraft

Siamak G. Hesar[1], Daniel J. Scheeres[2], Jay W. McMahon[3]
University of Colorado, Boulder CO 80309

Benjamin Rozitis[4]
The Open University, Milton Keynes, MK7 6AA, UK

A precise representation of small body surface thermal radiation pressure effects acting on orbiting spacecraft is discussed. The proposed framework takes advantage of a general Fourier series expansion to compute small body surface thermal radiation pressure. Fourier series expansion has been used before for the precise representation of solar radiation pressure effects on spacecraft orbiting small bodies. This framework takes into account the surface thermal parameters of small bodies, geometric relationship of orbiting spacecraft with the small body surface, and the shape and surface properties of spacecraft allowing for the computation of thermal radiation pressure, which may also be used for the generation of precise orbit determination solutions. After presenting the general model, we provide an example application of the model for the OSIRIS-REx spacecraft in orbit about Asteroid (101955) Bennu. Via simulation studies, we evaluate the effect of mis-modeling the thermal radiation pressure on the spacecraft and study the utilization of the proposed method for generating precise orbit determination solutions.

---

[1] Research Associate, Colorado Center for Astrodynamics Research, University of Colorado, Boulder CO 80309
[2] A. Richard Seebass Chair Professor, Department of Aerospace Engineering Sciences, University of Colorado, Boulder, CO 80309
[3] Assistant Research Professor, Department of Aerospace Engineering Sciences, University of Colorado, Boulder, CO 80309
[4] RAS Research Fellow, Planetary and Space Sciences, School of Physical Sciences, The Open University, Milton Keynes, MK7 6AA, UK

I. Introduction

In this paper we propose a framework for the precise representation of thermal radiation pressure acting of spacecraft orbiting small bodies. The framework takes into account the surface thermal parameters of small bodies, geometric relationship of orbiting spacecraft with the surface of a small body, and the shape and surface properties of spacecraft allowing for the precise computation of thermal radiation perturbing effects. The framework also utilizes a general Fourier series expansion of the perturbing force, which allows it to be used efficiently for the generation of precise orbit determination solutions. Fourier series expansion has been implemented for the precise representation of solar radiation pressure (SRP) effects on spacecraft orbiting small bodies in another study by the same authors [1].

Small body surface radiation pressure is due to the reflection and the emission of the sunlight energy intercepted by the asteroid or comet. The surface of small bodies interact with the incident sunlight and re-radiate a portion of that light either in the form of diffused and specular reflection, i.e. the albedo effect, or in the form of thermal radiation of the absorbed sunlight energy. The reflected and emitted radiation flux interact with the spacecraft surface much like the solar radiation flux and imparts a net force on the spacecraft. In general, the imparted force due to the thermal emission of the absorbed solar energy is much stronger than the albedo effect for asteroids and comets. Therefore, in this work, we refer to the small body surface radiation pressure (thermal emission and albedo effects combined) as small body thermal radiation pressure or TRP for short.

The TRP effect has been studied extensively for Earth orbiting spacecraft [2–5]. Even though the thermal radiation pressure effect is fairly small, its perturbing effects are documented on the orbits of Earth orbiting satellites [3, 6, 7]. Spacecraft orbiting a small body are also subject to TRP perturbations among numerous other perturbing forces, such as perturbations from non-uniform gravitational field, strong perturbing effects of solar radiation pressure, outgassing of the surface volatiles around a comet, and other forces such as errors in the maneuver executions or heat radiation pressure from the spacecraft components. Due to relatively weak gravitational attraction of small bodies, each one of these forces may impart considerable perturbation on the spacecraft orbit, and a precise orbit determination of spacecraft requires a precise model for these perturbing forces.

In this paper, we present a new model for the precise representation of TRP perturbing effects on spacecraft orbiting small bodies. The proposed framework draws from methods established by three different fields of research and puts together a uniform model for TRP effects on small body orbiting spacecraft. These serve as three main parts of the proposed framework, which are: 1) The geometry of the thermal radiation pressure effect on an orbiter that was formally introduced by Knocke et al. [2] for the computation of the Earth radiation pressure acting on Earth orbiting satellites; 2) Computation of the surface temperature of small bodies (asteroids and comets) that is studied extensively by Harris [8], Lebofsky et al. [9], and Spencer et al. [10] among others; 3) Fourier series expansion of the perturbing solar radiation pressure effects that was established by Scheeres [11], and this work implements this method for the efficient computation of the perturbing effects of thermal radiation pressure acting on spacecraft. In the next two sections, we further detail the ways in which we utilize these methods to assemble a framework for the precise computation of TRP effects on small body orbiting spacecraft.

II. Formulation of Thermal Radiation Pressure

A. Geometry of the TRP effect

Knocke et al. [2] developed the formulation for treating the Earth radiation pressure on Earth orbiting satellites. This formulation divides the surface of a spherical Earth into smaller surface elements and computes the radiation flux output from each surface element as a function of the incident sunlight angle and the surface temperature. The total albedo and thermal radiation flux from the surface is computed by aggregating the flux from each individual surface element. Figure 1 shows the geometry of this setup. As shown in this figure, $\mathbf{b}_j$ is the vector pointing from the center of the coordinate system to the centroid of the surface element j. Vector $\mathbf{u}_j$ is the vector pointing from the spacecraft to the centroid of that surface element. Angle θ_j is the angle between the incident sunlight and the j^{th} surface normal. Angle α_j is the angle between the incident sunlight and a vector pointing from the surface element j to the spacecraft, i.e. $-\mathbf{u}_j$. This model may be adapted to compute the radiation pressure imparted on spacecraft from the surface of small bodies. One thing to note is that the geometry given in Figure 1 is based on the assumption of an spherical

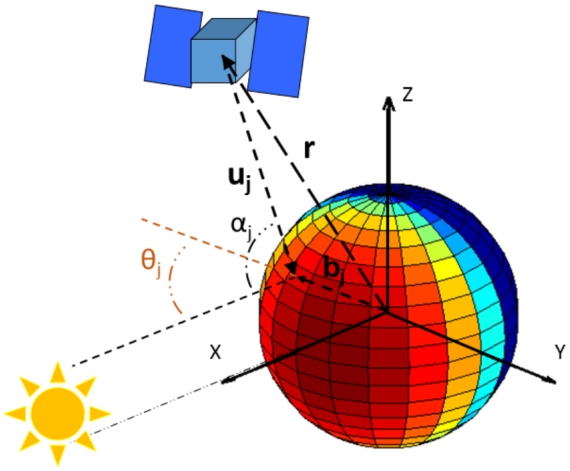

Fig. 1 Geometry of the surface radiation pressure model.

central body. For small bodies with highly non-spherical shapes this assumption does not hold. Nonetheless, this problem can be overcome rather easily by using a faceted shape model of a small body, such as the polyhedron shape model to apply the same formulation. In doing so, each facet (or a collection of facets) in the faceted shape model may be considered as a surface element in the TRP model.

In this work, we combine this model with the SRP formulation given by Scheeres [11] to derive the equations that express TRP effects on spacecraft in close proximity to a small body taking into account the shape of the spacecraft. We start the derivation by expressing the total force imparted on a spacecraft due to TRP as the following

$$\mathbf{F}_{TRP} = \sum_{j \in \mathcal{K}} P_j \sum_{i=1}^{N} \mathbf{f}_{ij}, \tag{1}$$

where the individual forces are summed across a total of N spacecraft irradiated surfaces and across all of the "effective" surface elements on the small body, which are in direct line-of-sight to the spacecraft. The set of effective surface elements are identified by the set $\mathcal{K}$. Variable P_j is the radiation pressure of the surface element j and $\mathbf{f}_{ij}$ is an area geometry function that describes the way the radiation from the surface element j is interacting with the spacecraft surface element i.

Using the notation from Scheeres [11], this force may be given by

$$\mathbf{f}_{ij} = -\left[\left(\rho_i s_i(2\hat{\mathbf{n}}_i\hat{\mathbf{n}}_i - \bar{\bar{U}}) + \bar{\bar{U}}\right)\cdot\hat{\mathbf{u}}_\mathbf{j}\hat{\mathbf{u}}_\mathbf{j}\cdot\hat{\mathbf{n}}_i + B(1-\rho_i s_i)\hat{\mathbf{n}}_i\hat{\mathbf{n}}_i\cdot\hat{\mathbf{u}}_j\right]H_i(\hat{\mathbf{u}}_j)A_i, \tag{2}$$

where the reflectivity ratio (albedo) of the spacecraft surface element i is given by ρ_i and its specular fraction is denoted by s_i. Vector $\hat{\mathbf{n}}_i$ is a unit normal vector pointing outward from the spacecraft surface i and $\hat{\mathbf{u}}_\mathbf{j}$ is the unit vector pointing from the spacecraft center to the centroid of that surface element j. Note that in defining this vector we make the assumption that the size of the spacecraft is very small compared to the distance of the spacecraft from the small body. As a result, we are able to use the same unit vector pointing from different surfaces of a spacecraft to a particular small body surface element. While this assumption helps simplify the formulation, it is not necessary. The quantity $\bar{\bar{U}}$ is the unity dyad and B is the Lambertian scattering coefficient of the surface (ideally equal to 2/3) [11]. Following Function $H_i(\hat{\mathbf{u}}_j)$ is defined as a visibility function that is equal to 1 if the surface element j is in view of the spacecraft surface element i and 0 otherwise. Note that this is in addition to the constraint that is placed on the effective surface element set $\mathcal{K}$. Finally, A_i is the surface area of the spacecraft surface element i.

Using Eq. (2) allows us to take into account the shape of a spacecraft when computing the TRP effect. This is one aspect where our derivation differs from the model provided by Knocke et al. [2], as they derive the equations of the TRP effect for a spherical spacecraft, i.e. a cannonball model. We derive the parameter P_j to be

$$P_j = \left(\tau_j a_j G_R\cos(\theta_j) + f_\epsilon(T_j)\right)\frac{1}{c}\cos(\alpha_j)\frac{A_j}{\pi u_j^2}, \tag{3}$$

where τ_j is the visibility function of the surface element j with respect to the sunlight, i.e. τ_j is equal to 1 if that surface element is lit by the sunlight and 0 otherwise. Variable a is the albedo of the body, which is defined as the fraction of the shortwave radiation reflected from the surface of the body to the incident shortwave solar radiation [12] (§ 3.7.1). Here we assume a constant albedo across the entire surface of the body, however one may easily define different albedo values for different surface elements as suggested by the subscript j. Variable G_R is the solar flux at the distance R from the Sun (= 1368 $Js^{-1}m^{-2}$ at 1AU) [13] and c is the speed of light. Variable A_j is the surface area of the surface element j and u_j is the distance of the spacecraft to that surface

element. Finally, the function $f_\epsilon(T_j)$ indicates the amount of thermal radiation flux emitted from the surface element j that has a surface temperature of T_j. The actual form of this function is another aspect that our derivation differs from the model given by Knocke et al. [2]. More details on this are provided in Section II B.

B. Asteroid Surface Temperature Distribution

Many of the previous models that are developed for the Earth radiation pressure assume an emissivity function $f_\epsilon(T_j)$ that is strictly latitude dependent [2–4]. Stephen et al. [5] shows that the terrestrial emissivity function may be modeled adequately by only using the zonal spherical harmonics up to degree 2. However, studying asteroids' surface temperature distribution using observational data supports the idea that there exists a pronounced temperature variation that has a strong latitudinal and longitudinal dependency [14]. Therefore, it is most appropriate to discretize the emissivity across the surface elements. For a surface element with temperature T_j the emissivity function $f_\epsilon(T_j)$ may be given by

$$f_\epsilon(T_j) = \epsilon \sigma_B T_j^4, \tag{4}$$

where ϵ is the surface emissivity of the body and $\sigma_B = 5.670367 \times 10^{-8}\ W/m^2/K^4$ [15] is the Stefan Boltzmann constant. Hence, for a given temperature map on the asteroid surface, one can compute the corresponding emissivity function. The popular Near-Earth Asteroid Thermal Model (NEATM) [8], and an earlier version of it called the standard thermal model (STM) [9], adopt the following expression to compute the temperature distribution on the surface of an asteroid:

$$T(\imath) = \begin{cases} T_{SS} \cos^{1/4}(\imath) & 0 \leq \imath \leq \pi/2 \\ 0 & \imath > \pi/2 \end{cases}, \tag{5}$$

where $\imath$ is the angular distance from the subsolar point and T_{SS} is the subsolar temperature that is given by

$$T_{SS} = \left(\frac{(1 - a_b) G_R}{\epsilon \sigma_B} \right)^{1/4}, \tag{6}$$

where a_b is the Bond albedo of the asteroid. In the literature [8, 16, 17], a so called *beaming parameter* is included in the denominator of Eq. (6). This is an empirical parameter that was devised to help

the model better match the observed flux data and does not reflect the actual surface temperature on the asteroid [10]. In this work, we choose to disregard this parameter as we are interested in the actual value of the temperature on the surface.

The NEATM assumes that the peak temperature occurs at the subsolar point on the surface of an asteroid and the temperature decreases with the increased angular distance away from this point. This is equivalent to an assumption of a zero thermal inertia for an asteroid, such that an instantaneous thermal equilibrium occurs on its surface. The fast rotating model (FRM) [18] is another variation to the NEATM. This model assumes a very large value for the thermal inertia, such that the surface temperature is constant across different longitudes and is only a function of the latitude. However, in reality, for an asteroid with a finite thermal inertia, the surface temperature is not constant across different longitudes and the peak temperature occurs at an angular distance – *phase angle* – away from the subsolar point towards the evening side. A work by Spencer et al. [10] developed a so called *thermal parameter* (Θ) that combines the rotation rate, thermal inertia, and the possible peak surface temperature of an asteroid to characterize the temperature distribution on the surface. This parameter is given by [10]

$$\Theta = \frac{\Gamma\sqrt{\omega_r}}{\epsilon\sigma_B T_{SS}^3}, \tag{7}$$

where Γ is the thermal inertia and ω_r is the rotation rate of the asteroid. Note that the thermal parameter is a dimensionless quantity. A $\Theta = 0$ corresponds to the NEATM, while a $\Theta = \infty$ corresponds to the FRM. By solving a boundary value problem Spencer et al. [10] generated a set of reference curves for the maximum and minimum surface temperatures and the phase angle as a function of the thermal parameter Θ. These curves are depicted in Figure 2 *. Using Eq. (7) and (6) one may compute the thermal parameter for an arbitrary asteroid and then use Figure 2 to identify the corresponding maximum and minimum surface temperatures and the phase angle. Plugging these values in Eq. (5) results in a simplified description of the surface temperature distribution of the given asteroid. Note that this model assumes a spherical model of the asteroid with an obliquity

* Reprinted from Icarus, Vol. 78, Issue 2, J. R. Spencer, L. A. Lebofsky, and M. V. Sykes, Systematic biases in radiometric diameter determinations, Pages 337-354, Copyright (1989), with permission from Elsevier, under the License No. 3973730079280.

of 0 degrees.

For the simulation studies presented in this paper, we use a numerical method that solves for 1-D heat conduction [19, 20] with a spherical shape and zero obliquity assumptions for Bennu. For temperature T, time t and depth z, 1-D heat conduction for a surface element is described by

$$\frac{\partial T}{\partial t} = \frac{k}{\sigma C}\frac{\partial^2 T}{\partial z^2}, \tag{8}$$

where k is the thermal conductivity, σ is the material density, and C is the heat capacity. These properties combine to give the thermal inertia as $\Gamma = \sqrt{k\sigma C}$. To ensure conservation of energy between absorbed solar flux, conducted heat, and emitted thermal radiation, a suitable surface boundary condition is given by

$$(1 - a_b)G_R \cos(i(t)) + k\left(\frac{\partial T}{\partial z}\right)_{z=0} - \epsilon\sigma_B T^4_{z=0} = 0 \tag{9}$$

where the incidence angle $i(t)$ is a function of time appropriate for the latitude band of the surface element of interest. A numerical finite-difference technique is then used to solve the 1-D heat conduction equation, and a Newton-Raphson iterative technique is used to solve the surface boundary condition. The asteroid rotation is resolved into 720 time steps, and the asteroid surface layer is resolved into 56 depth steps going down to a maximum depth of 8 thermal skin depths. Zero temperature gradient is also assumed at this maximum depth to give a required internal boundary condition. For specified asteroid properties, the model is run over a suitable number of asteroid revolutions until the surface temperatures converge to stable values between successive revolutions. This is then repeated for each surface element to be modeled on the asteroid.

III. TRP Fourier Series Representation

A. General Formulation

Previous research [11] has implemented a general Fourier series expansion for the precise representation of SRP effects. This method reduces the shape and the surface properties of an object, e.g. a spacecraft, down to a list of coefficients that form an infinite Fourier series expansion. While the values that are computed for such coefficients are specific for a given shape and surface properties of a spacecraft, their treatment within the Fourier expansion is general. This method is akin to

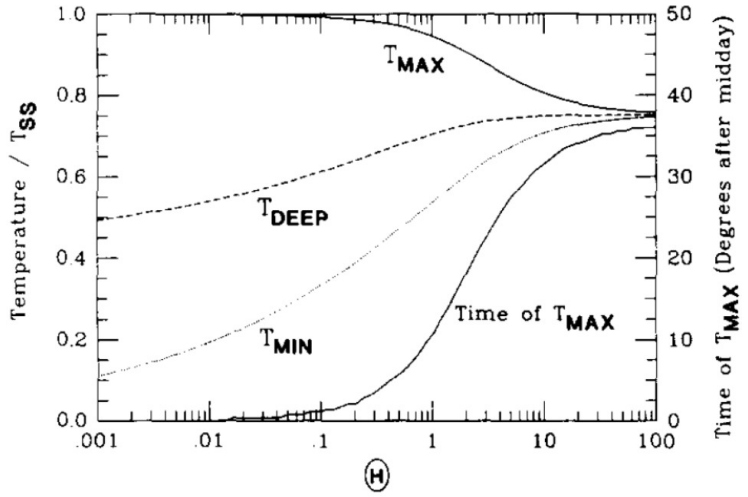

Fig. 2 The maximum (T_{max}) and minimum (T_{min}) surface temperatures and the subsurface (T_{DEEP}) temperature of an asteroid as a function of the thermal parameter Θ. The figure also shows the time of maximum temperature as the number of degrees after midday.

representing the gravitational field of an object via a spherical harmonics expansion with its corresponding spherical harmonics coefficients. This method was developed by Scheeres [11] to model the dynamical evolution of asteroids' motion due to the Yarkovsky–O'Keefe–Raszievskii–Paddack or "YORP" effect [21, 22]. It was later expanded to represent the SRP effects on spacecraft [23–27].

There are certain advantages to using a Fourier series expansion to model SRP effects on spacecraft. First, it allows for an efficient and computationally inexpensive way to include the information regarding the shape and the surface properties of a spacecraft in the computation of the perturbing forces. It is also suitable for the use in an orbit determination (OD) process as the coefficients of the model may be estimated during the time that spacecraft is in orbit to improve the OD solutions [28]. In this work, we extend the general Fourier series expansion to model the force imparted on spacecraft due to TRP. First, we review the formulation of the model in a more general sense before applying it to the OSIRIS-REx spacecraft example. The Fourier series representation of the TRP force is given by

$$\mathbf{F}^b_{TRP} = \sum_{j\in\mathcal{K}} P_j \sum_{n=0}^{\infty} \left[\mathbf{A}_n(\delta_j)\cos(n\lambda_j) + \mathbf{B}_n(\delta_j)\sin(n\lambda_j)\right], \tag{10}$$

where δ_j and λ_j are the latitude and the longitude of asteroid surface element j in a specified refer-

ence frame. In general, it is preferred to compute this force in the spacecraft body-fixed coordinate frame, as denoted by the b superscript. Hence, coefficients $\mathbf{A}_n(\delta_j)$ and $\mathbf{B}_n(\delta_j)$ are vectors of 3 components expressed in this frame. The Fourier coefficients defined in the spacecraft body-fixed frame are time invariant functions of the radiation source line-of-sight latitude. These coefficients may be computed from a given shape model of a spacecraft and its corresponding surface properties via the following equations [11]

$$\mathbf{A}_0(\delta_j) = \frac{1}{2\pi} \int_0^{2\pi} \frac{\mathbf{F}_j}{P_j}\, d\lambda_j,$$

$$\mathbf{A}_n(\delta_j) = \frac{1}{\pi} \int_0^{2\pi} \frac{\mathbf{F}_j}{P_j} \cos(n\lambda_j)\, d\lambda_j, \text{ and} \tag{11}$$

$$\mathbf{B}_n(\delta_j) = \frac{1}{\pi} \int_0^{2\pi} \frac{\mathbf{F}_j}{P_j} \sin(n\lambda_j)\, d\lambda_j,$$

where $\mathbf{F}_j = P_j \sum_{i=1}^{N} \mathbf{f}_{ij}$. Note that $\mathbf{f}_{ij}$ is only a function of the shape and surface properties of the spacecraft. Finally, the produced acceleration due to this force is easily given by

$$\mathbf{a}_{TRP}^b = \frac{1}{m_{SC}} \sum_{j \in \mathcal{K}} P_j \sum_{n=0}^{\infty} \left[\mathbf{A}_n(\delta_j) \cos(n\lambda_j) + \mathbf{B}_n(\delta_j) \sin(n\lambda_j) \right], \tag{12}$$

where m_{SC} is the mass of the spacecraft. While the spacecraft body-fixed frame is the preferred reference frame for this formulation, it is not a suitable reference frame for many of the analyses involving orbit elements of the spacecraft and spacecraft navigation. An inertial reference frame is normally used to perform spacecraft orbit determination. In general, one may use a mapping matrix Ψ to map the TRP acceleration from the spacecraft body-fixed frame to another reference frame. The mapping expression is given by

$$\mathbf{a}_{TRP} = \Psi \mathbf{a}_{TRP}^b, \tag{13}$$

where the actual form of the matrix Ψ depends on the frame of choice that $\mathbf{a}_{TRP}$ is expressed in.

B. Numerical Simulations for the OSIRIS-REx spacecraft

Having defined the general formulation for the TRP model, we present numerical simulations that implement the proposed method for a simulated OSIRIS-REx spacecraft in orbit about Asteroid

(101955) Bennu. A simple box-wing model of the spacecraft that is depicted in Figure 3 is used for this simulations. Surface properties of the spacecraft surface elements are summarized in Table 1.

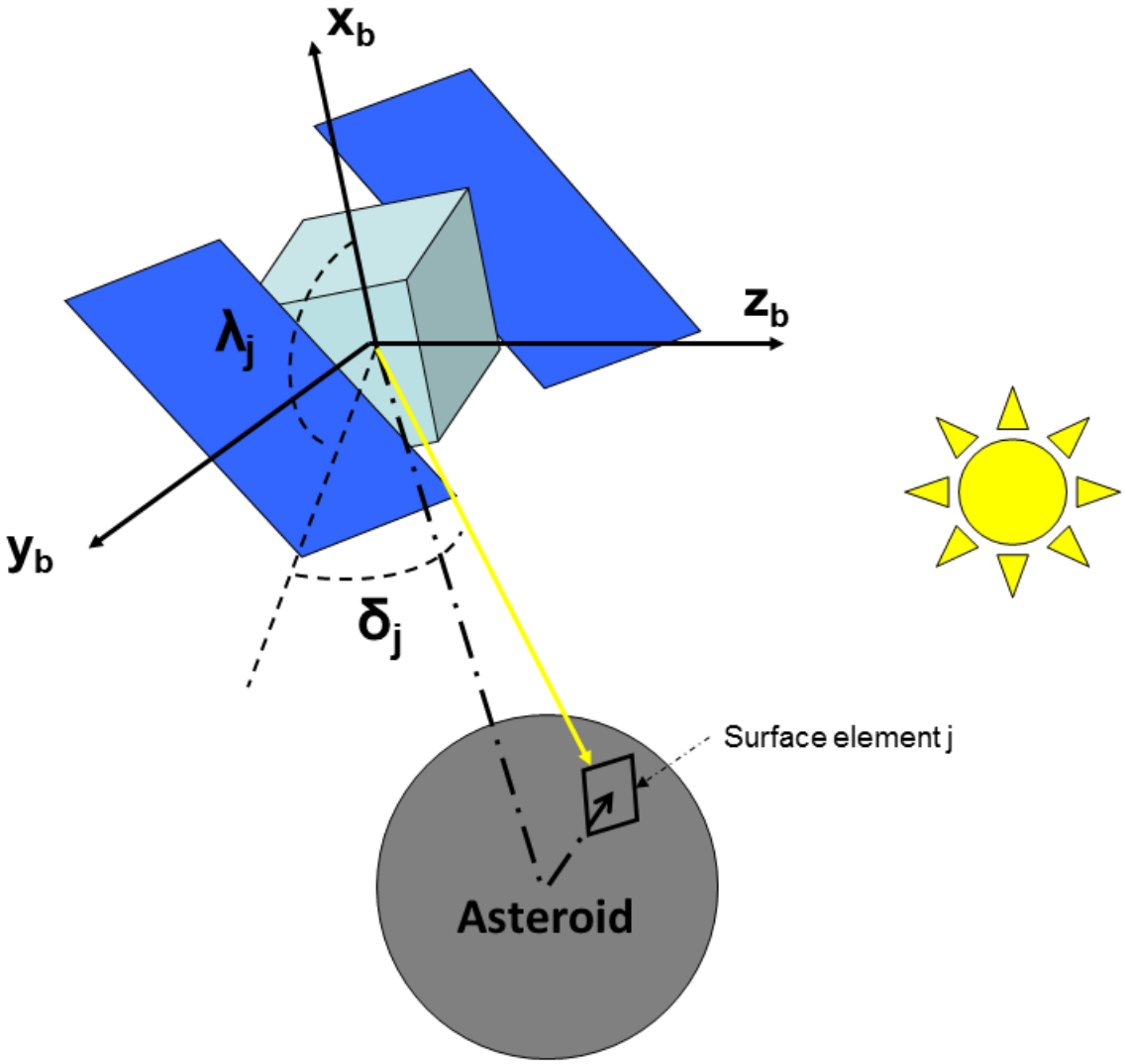

Fig. 3 Spacecraft box-wing model and a view of a surface element coordinates in the spacecraft body-fixed frame.

The coordinates in the table are aligned with the spacecraft body fixed frame given by Figure 3. These surface properties are used to compute the nominal values of the Fourier coefficients for our example. One can relate the surface properties given in Table 1, namely the C_s and C_d, to those

Table 1 Surface properties for a 10-plate box-wing model of the OSIRIS-REx spacecraft.

	Normal vector			Surface properties		
	$\hat{\mathbf{x}}^b$	$\hat{\mathbf{y}}^b$	$\hat{\mathbf{z}}^b$	Specular Coeff. C_s	Diffused Coeff. C_d	Area (m^2)
+x bus	1	0	0	0.056	0.435	6.471
-x bus	-1	0	0	0.000	0.440	6.471
+y bus	0	1	0	0.076	0.411	5.175
-y bus	0	-1	0	0.076	0.411	5.175
+z bus	0	0	1	0.000	0.473	5.174
-z bus	0	0	-1	0.000	0.473	5.174
-y solar panel Front	0.707	0	0.707	0.080	0.000	4.903
+y solar panel Front	0.707	0	0.707	0.080	0.000	4.903
-y solar panel back	-0.707	0	-0.707	0.000	0.070	4.903
+y solar panel back	-0.707	0	-0.707	0.000	0.070	4.903

introduced by Eq. (2) using the following relationships

$$\begin{aligned} C_s &= \rho s, \\ C_d &= 1 - \rho s. \end{aligned} \tag{14}$$

Although we consider a simple shape model for this study, the remarkable fact about this formulation is that Fourier coefficients may be pre-computed in the same fashion for any level of complexity of a spacecraft shape model without affecting the amount of the computation required during a numerical propagation or an orbit determination process.

Figure 4 shows a comparison of the TRP acceleration computed by the box-wing plate model (the assumed true value for this simulation) and the Fourier series representation with different degrees of expansion. The simulated spacecraft is assumed to be in a circular terminator orbit about Bennu with an orbit radius of 1 km following a nadir-pointing attitude profile. The TRP force is generated using 648 surface elements on the asteroid; that is a surface mesh with a 10-degree resolution in latitude and longitude of a spherical asteroid model. The surface temperature distribution is computed using the numerical method described in Section II B. The asteroid is assumed to be at its perihelion for the generation of the surface temperature distribution. Other

assumed surface properties and the rotation rate of Bennu are given in Appendix A. The resulting surface temperature is shown in Figure 5(a). For the sake of comparison, we also compute he surface temperature profile via the analytical method given by Eq. (5) and taking into account the thermal parameter of the asteroid. This temperature profile, however, is not used in the simulation studies presented here. Using Eq. (7) we compute a thermal parameter of $\Theta = 1.6$ for Bennu. A phase angle of 17° towards the evening side from the sub-solar point is chosen for Bennu as it corresponds to the thermal parameter of $\Theta = 1.6$ according to Figure 2. The maximum and the minimum surface temperatures are also located from this figure. Figure 5(b) shows the temperature distribution given by this simple analytical method. Both methods show a similar temperature profile on the surface of Bennu. However, note that both of these methods make the simplifying assumption of a spherical asteroid. Other more sophisticated methods, such as those given in References [19, 20], may be used to generate a more accurate representation of the surface temperature profile of an asteroid taking into account its shape and orientation is space. Having said that, due to the discretized nature of the proposed TRP model, any one of such methods may be easily implemented without a need to modify the model.

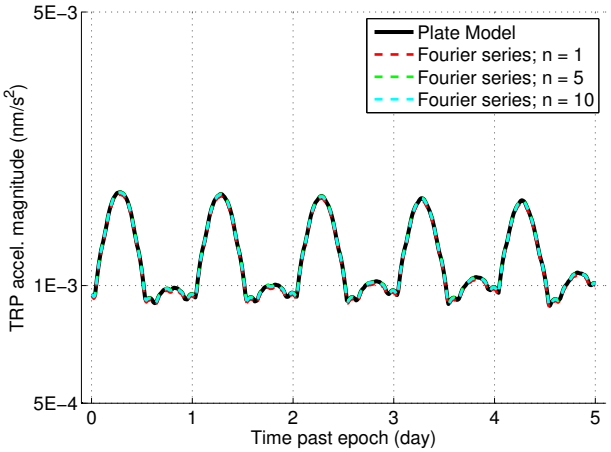

Fig. 4 A comparison of the plate model vs. the Fourier series expansion for the computation of the TRP acceleration.

Figure 4 shows that a 1st degree Fourier series expansion is able to provide a close approximation of the the true value of the TRP acceleration profile. Increasing the expansion degree from 1 to

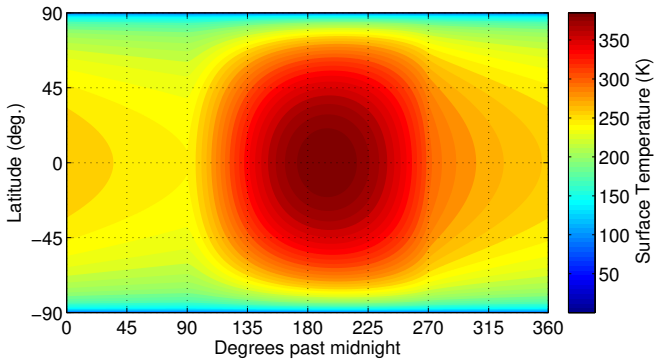

(a) Numerical method

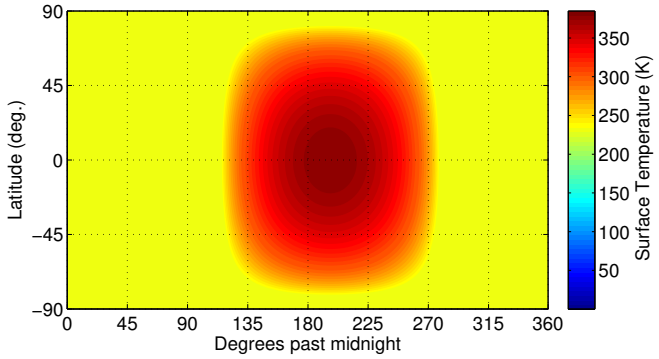

(b) Analytical method

Fig. 5 Simulated temperature distribution on the surface of Bennu.

higher degrees will fine tune the way the true TRP effect is captured. This is clear from Figures 4 as one can not easily distinguish the difference between the TRP acceleration magnitude given by a degree 5th expansion, a degree 10th expansion, and the true signal.

Figure 6(a) shows a comparison of the SRP and TRP accelerations for the 1 km terminator orbit. At a distance of about 750 meters (1 km orbit radius) from the surface the magnitude of the TRP acceleration is about 2 orders of magnitude smaller than that for the SRP acceleration. The orbit being on the terminator plane contributes to the weak TRP effect, since the spacecraft is not directly exposed to the hotter sunlit side of the asteroid surface. To analyze this further, Figure 6(b) shows the average TRP acceleration magnitude along a circular terminator orbit with different radii. This figure shows that by decreasing the orbit radius by a half, the average TRP magnitude increases by a factor of 4, from about 1.2% to about 4.8% of the magnitude of the SRP acceleration. This is an intuitive results as the intensity of the TRP acceleration is inversely related

to the square of distance of spacecraft from the asteroid surface.

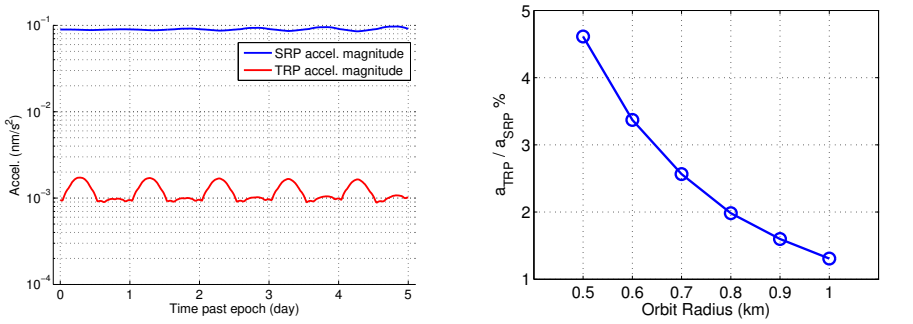

(a) TRP and SRP at a 1 km circular terminator orbit

(b) TRP acceleration vs. terminator orbit radii

Fig. 6 Comparison of TRP and SRP effects on OSIRIS-REx spacecraft in orbit about Bennu

A TRP acceleration magnitude of about 1% to 5% of the SRP acceleration is a small amount that may not be of much importance. However, for other trajectories that come close to the surface of the asteroid on the sunlit side, the TRP effect would be more pronounced. For instance, this is the case for the TAG rehearsal and TAG departure trajectories of the OSIRIS-REx mission, where the spacecraft is planned to fly over the designated TAG site from a distance of about 125 meters above the asteroid surface on the sunlit side [29]. Figure 7 shows a simulated TAG rehearsal trajectory of the spacecraft that starts from a 1 km circular terminator orbit and passes through a check point that is 125 meters above the planned TAG point at the -45° latitude. Figure 8 shows the TRP and the SRP acceleration profiles along this trajectory. As shown on this plot, at the maximum point the intensity of the TRP acceleration may increase up to about 20% of the SRP acceleration magnitude. This is a potentially strong perturbation that may have a notable adverse effect on orbit determination solutions and spacecraft uncertainty propagation, if it is not modeled properly.

IV. TRP Effects on Precise Orbit Determination Solutions

Section III showed that, in general, TRP accounts for only a small percentage of the perturbing forces that are imparted on a spacecraft orbiting a small body. However, its effect may become more noticeable when generating a precise OD solution or when propagating the uncertainty of an OD

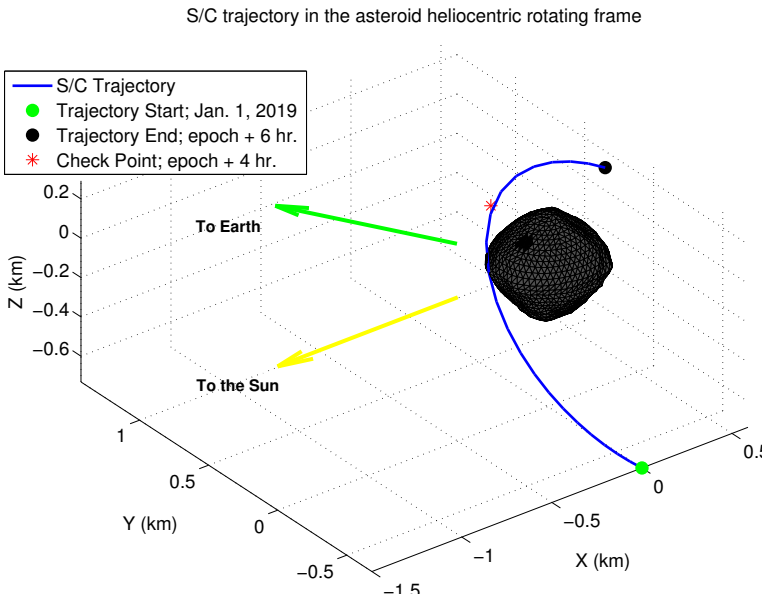

Fig. 7 A simulated TAG rehearsal trajectory for the OSRIRIS-REx spacecraft about Bennu.

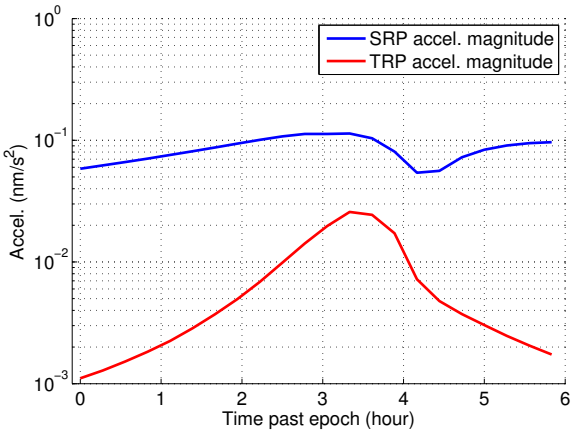

Fig. 8 The TRP and the SRP acceleration magnitudes along the simulated TAG rehearsal trajectory.

solution for a long time span. In this section, we perform two sets of simulation studies to evaluate the effects of not modeling or mis-modeling of TRP on OD solutions.

A. Case I simulation: TAG rehearsal trajectory OD

First, we study navigating a simulated OSIRIS-REx spacecraft during its TAG rehearsal trajectory that is shown in Figure 7. As mentioned in Section III the force imparted on the spacecraft due to TRP may increase up to 20% of the SRP effect. Hence, we are interested in quantifying the

effect this force might have in the navigation solution during this trajectory.

1. Dynamical Model

The truth trajectory of the simulation is shown in Figure 7, where the spacecraft starts from a 1 km circular terminator orbit and passes through a check point, which is 125 meters above the TAG point at the -45° latitude after 4 hours and continues for 2 more hours in that trajectory. The force model used for generating this trajectory is shown in Table 2. Note that both the SRP and TRP are computed using the 10-plate box-wing model for the truth trajectory. The spacecraft is assumed to be in a nadir-pointing attitude during this trajectory. The truth trajectory is used to generate simulated optical and DSN measurements according to the measurement model discussed in the following section.

Table 2 The truth force model used in the simulation studies

Simulation Epoch:	2019 Jan 10 18:42:10.321 TDB
Force Model	
Central Body:	Bennu ($\mu = 5.2\ m^3/s^2$) [30]
Gravity Model:	16×16 spherical harmonics expansion
SRP:	10-plate model (see Figure 3)
TRP:	10-plate model (see Figure 3)
Third body:	Sun (point mass)

2. Measurement Model

We process a combination of simulated optical landmark measurements from the surface of the asteroid as well as simulated radiometric measurements between three simulated DNS antennas and a spacecraft. Optical landmark observations consist of a set of sample and line measurements from a total of 100 landmarks that are selected randomly on the surface of the asteroid. A fairly wide-angle camera is assumed to be mounted on the spacecraft with a focal length of about 12 mm and a 30° field of view (FOV) with a 512×512 pixels array. Landmarks go in and out of the camera FOV as the orbiter goes around the asteroid and as the asteroid rotates about its rotation axis. A 2° limit above the horizon determines when a landmark is in view of the camera, given that it falls

within the FOV limit of the camera and that it is illuminated by the sunlight. The radiometric observations are simulated as idealized range and range-rate measurements between DSN antennas and the simulated spacecraft. Three DSN antennas are chosen for simulating these measurements, namely DSS14 in Goldstone, CA, DSS43 in Canberra, Australia, and DSS63 in Madrid, Spain. A local antenna mask of 10° above the horizon is applied to the DSN antennas when generating the measurements. The observations are generated when the line-of-sight between a DSN antenna and the spacecraft is not occulted. The landmark sample and line observations are generated once

Table 3 Measurement errors

Measurement	Measurements weighting
Sample and Line	0.25 pixels
DSN Observations	
Range	3 meter
Range-rate	0.1 mm/sec

every 5 minutes continuously (whenever a landmark is in view of the camera and is lit). The DSN radiometric observations are collected once every 1 minute. Table 3 summarizes the measurement errors that are used in this study.

For the simulations presented here, the navigation camera is assumed to be pointing towards the center of Bennu during the entire arc. Figure 9 shows the number of visible simulated landmarks and the spacecraft altitude during the TAG rehearsal trajectory, which shows that the number of the visible landmarks decrease as the spacecraft comes closer to the asteroid surface and vanish on the night side of the body.

3. Orbit Determination Setup and Results

The estimated parameter set in this simulation is the spacecraft state with 10 meters of *a priori* uncertainties in the position and 10 cm/sec in the velocity in all three cartesian directions. Two sets of Monte-Carlo simulations are performed for this study, one that includes the TRP effect in the filter model and another one that does not. For each set we run 300 cases. For each case, the initial state of the spacecraft is perturbed from the truth state by an error generated from

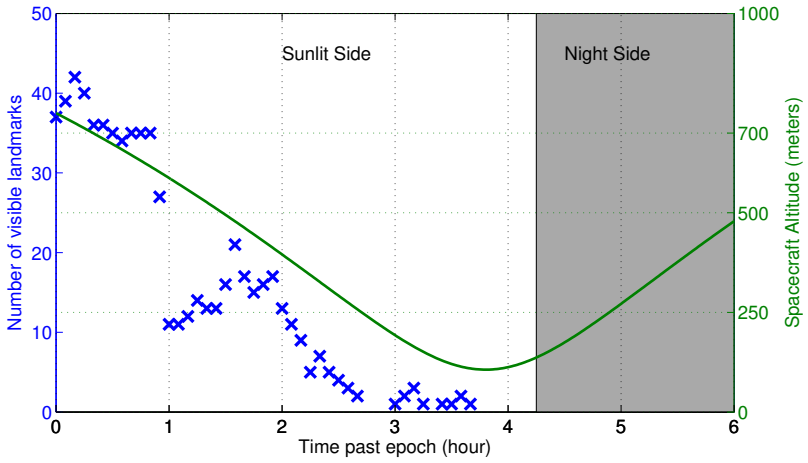

Fig. 9 Number of visible landmarks and the spacecraft altitude during TAG rehearsal trajectory.

a Gaussian distribution of zero mean and a standard deviation of 10 meters in the position and 10 cm/sec in the velocity at each direction. Available landmark measurements are processed once every 5 minutes, while the DSN range and range-rate measurements are processed once every 1 minute during each simulation. Measurement noise is added to the simulated observations for each simulation run according to the noise levels indicated in Table 3. The parameters of the filter dynamical model are summarized in Table 4. No process noise is added for the case where the TRP effect is not included in the filter model. This helps isolate the effect of mis-modeling of TRP on the OD solution. The partial derivatives of the filter dynamical model and the measurement model with respect to the estimated state parameters are detailed in Reference [28]. Table 5 summarizes

Table 4 Filter Model for the Simulations

Simulation Epoch: 2019 Jan 10 18:42:10.321 TDB	
Filter Force Model	
Central Body:	Bennu ($\mu = 5.2\ m^3/s^2$)
Gravity Model:	16×16 field
SRP:	Fourier expansion n = 10
TRP:	Fourier expansion n = 10 (if included)
Third body:	Sun (point mass)

the results of the 300 Monte Carlo filter runs for each of the simulation cases, with and without the TRP effect.

As shown in these results, the weighted RMS of the observations for both cases is close to unity meaning that the filter is able to extract most of the signal from the observations. However, the RMS values show that the filter is performing slightly better for the case that TRP effect is included in the force model. This is more pronounced in the accuracy of the filter, where the 3D-RMS of the position accuracy is about twice as large for the case that does not include the TRP effect. Spacecraft velocity estimate accuracy is also improved by including the TRP effect in the filter. The reason that the mis-modeling of the TRP effect is not easily noticeable in the observation RMS values is due to the short observation arc and the large observation noise compared to the magnitude of the TRP signal. We explored this further in the second set of the simulation studies (see Section IV B) by processing longer observation arcs. The 3D-RMS of the accuracy, however, clearly shows that mis-modeling of the TRP has a negative effect on the accuracy of the estimated state. Figure 10 shows the accuracy plots of one sample simulation run (out of the 300 runs) in the radial (R), in-track (I), and cross-track (C) directions with and without including the TRP in the filter model. The initial errors and the measurement noise components are the same for both cases. This figure shows that the accuracy of the state estimate quickly falls out of 3σ uncertainty bounds for the case that does not include the TRP effect in the filter model (see Figure 10(b)), while it remains close to zero and within the uncertainty envelopes for the other case, as seen in Figure 10(a).

Table 5 Summary of the Monte Carlo filter analysis for the TRP effect.

	Landmark weighted RMS		DSN weighted RMS		3D-RMS	
	Sample	Line	Range	Range-rate	Position (m)	Velocity (mm/s)
With TRP	1.030	1.021	1.004	1.047	0.187	0.06
Without TRP	1.064	1.058	1.006	1.086	0.255	0.09

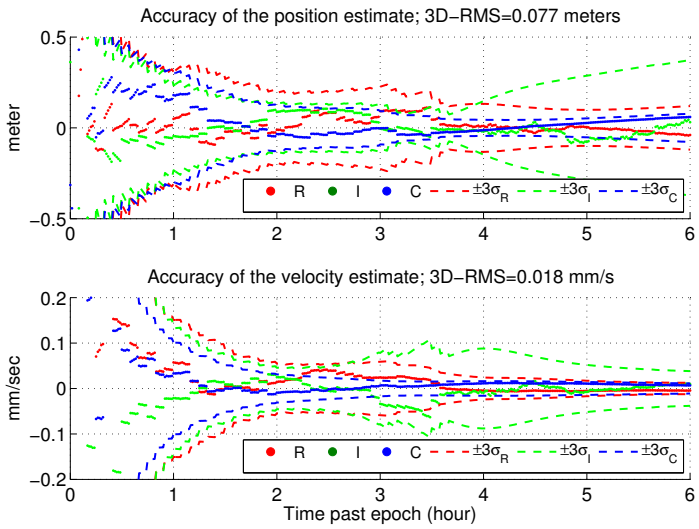

(a) TRP effect is modeled in the filter.

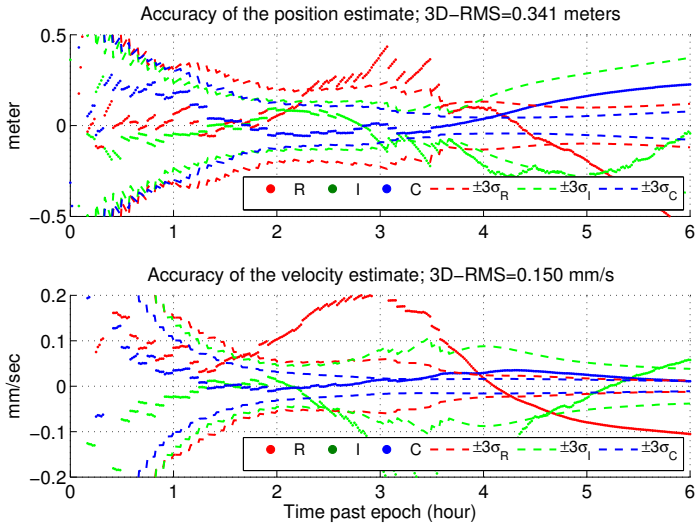

(b) TRP effect is not modeled in the filter.

Fig. 10 Accuracy plots of the spacecraft position estimate for a sample simulation run for Case I simulations.

B. Case II simulation: Terminator Orbit OD

The Case II simulation considers processing a longer observation arc and assessing the TRP effect on the OD solution. The truth trajectory for this simulation is a 1 km circular terminator orbit about Bennu. The truth and filter models are the same as those used in the previous study (Case I simulation). The truth trajectory is propagated for two days and the optical landmark and DSN radiometric observations are generated based this truth trajectory. The observations are

generated in the same fashion that was described in Section IV A 2. The estimated parameters are the spacecraft position and velocity vectors. The measurement noise, the state *a priori* uncertainties, and the state initial errors are the same as those given for the simulations in the previous section. Two filters are considered for this simulation, one that includes the TRP effect, and another one that does not. For the filter that dose not include the TRP effect we include a first order Gauss-Markov process noise [31] with a correlation time of 1000 seconds and a noise level of $\sigma = 1E-4\ nm/s^2$ in the radial direction and $\sigma = 5E-5\ nm/s^2$ in the in-track and cross-track directions. The process noise is used to compensate for the un-modeled TRP effect so that the filter does not diverge during the long arc.

The filtering strategy for this simulation is such that we run the filters for 1 day and compute the best estimate state of the spacecraft. The spacecraft trajectory is then propagated forward in time for one more day based on best estimate state given by the filter. During the 2nd day of the propagation, the measurement residuals are computed without updating the spacecraft state. This process is sometimes referred to as a "*pass-through*". Pass-through residuals are used to help validate a filter solution. The presence of large signals in the pass-through residual plots is an indication of the existence of mis-modelings in the dynamics that the filter is not able to resolve. Figures **??** and **??** show the pass-through residuals for the first filter results. For the second filter these residuals are shown in Figures **??**, and **??**. These results show a clear signal in the pass-through residuals due to the mis-modeling of the TRP effect in the second filter, which does not exists in the first filter results. These results show that, although very small, the TRP effect is clearly detectible via a precise orbit determination solution and it can affect the precision of the projected filter solutions. Additionally, the results show that using a Fourier series expansion for modeling the TRP, one is able to generate precise orbit determination solutions that are valid for long time spans, when propagated into the future.

V. Conclusion

A new model for precise representation of small body thermal radiation pressure is presented with an example application for the OSIRIS-REx spacecraft in orbit about Bennu. This model uses

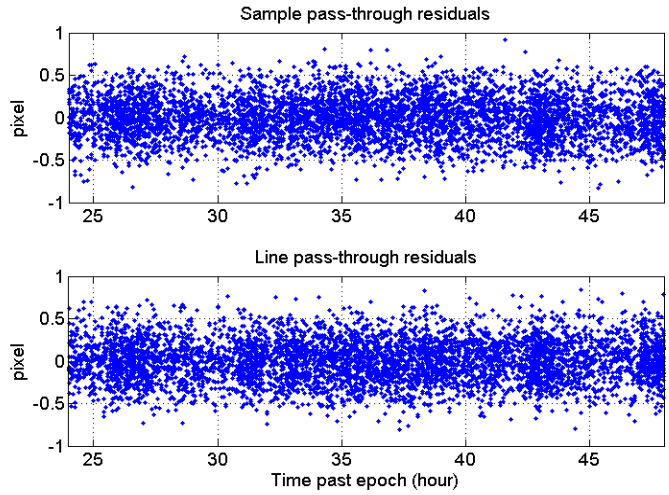

Fig. 11 Case II: Pass-through residuals of the OpNav measurements for the 1st filter results.

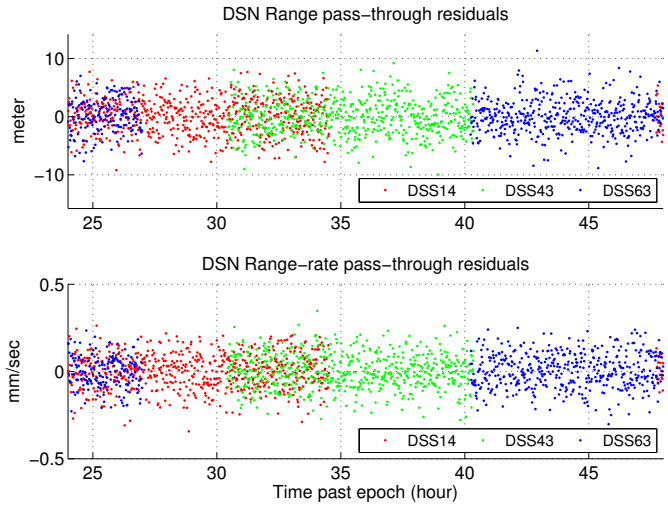

Fig. 12 Case II: Pass-through residuals of the DSN measurements for the 1st filter results.

a Fourier series expansion for the computation of surface radiation pressure effects on spacecraft taking into account the shape and the surface properties of spacecraft. We show that the Fourier series expansion is able to accurately represent TRP effects. A comparison of the magnitudes of TRP and SRP effects on the OSIRIS-REx spacecraft showed that while TRP is a very small source of perturbation ($\approx 1\%$ of SRP) for orbits that are relatively far from the surface of the asteroid ($\approx$ 1 km in radius), its effect becomes more pronounced as the spacecraft passes close to the surface of Bennu over its sunlit side. TRP effects may rise up to about 20% of SRP during the OSIRIS-REx

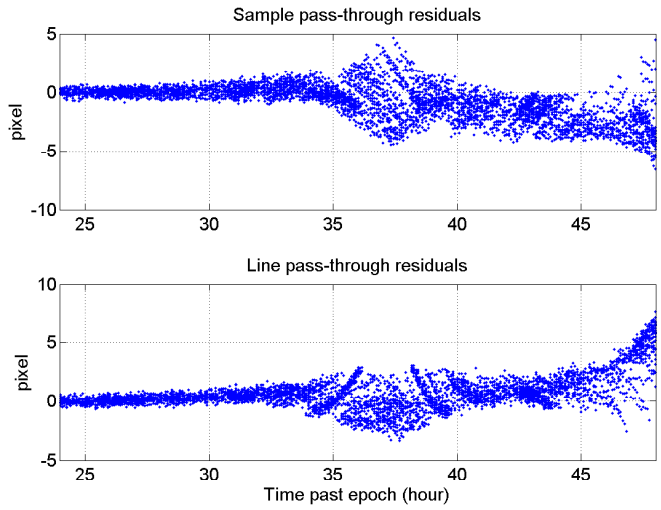

Fig. 13 Case II: Pass-through residuals of the OpNav measurements for the 2nd filter results.

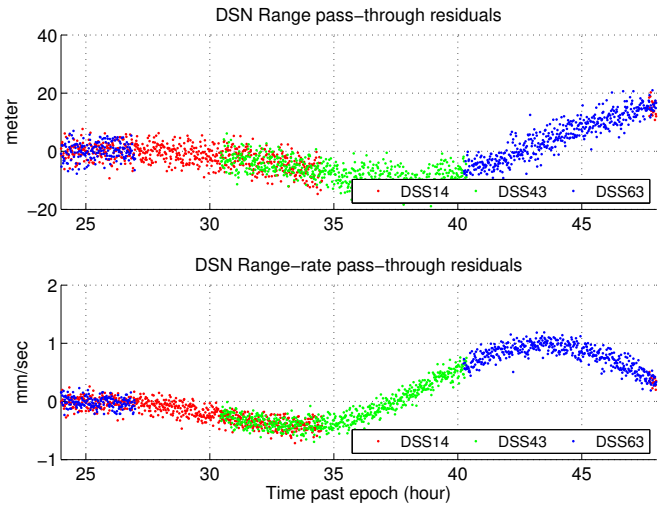

Fig. 14 Case II: Pass-through residuals of the DSN measurements for the 2nd filter results.

TAG rehearsal and departure trajectories. Furthermore, the study shows that mis-modeled TRP may have a notable effect on an OD solution especially for a trajectory that is close to the surface of the central body. Using the Fourier series representation of the TRP removes such mis-modeling and produces precise OD solutions that are valid for long propagation times.

Acknowledgement

The research and writing of this paper was supported by NASA contract NNM10AA11C (D. S. Lauretta, PI) and related subcontracts from the University of Arizona. BR acknowledges support from the Royal Astronomical Society (RAS) in the form of a research fellowship. The authors also thank the anonymous reviewers for their insightful comments that improved the paper.

APPENDIX A: PHYSICAL PARAMETERS OF ASTEROID (101955) BENNU

Table 6 summarizes the relevant physical parameters for Bennu [30].

Table 6 Summary of the physical parameters for Bennu

Gravitational parameter (μ):	$5.2 \pm 0.6\, m^3/s^2$
Rotation period:	4.29746±0.002 hr.
Thermal inertia (Γ):	$310 \pm 70\ J\, m^{-1} s^{-0.5} K^{-1}$
Surface emissivity:	0.90 ± 0.05
Bond albedo:	0.017 ± 0.002
Geometric albedo:	0.04 ± 0.002

REFERENCES

[1] Hesar, S., Scheeres, D., and McMahon, J., "Precise Solar Radiation Pressure Models for Small Body Orbiters: Applications to OSIRIS-REx," *submitted to the Journal of Guidance, Control, and Dynamics*, Under review.

[2] Knocke, P., Ries, J., and Tapley, B., "Earth radiation pressure effects on satellites," *Proceedings of the AIAA/AAS Astrodynamics Conference*, AIAA 88–4292, Minneapolis, MN, August 15–17, 1988, pp. 577–587.
doi: 10.2514/6.1988-4292

[3] Lautman, D. A., "Perturbations of a close-Earth satellite due to sunlight diffusely reflected from the Earth," *Celestial mechanics*, Vol. 15, No. 4, 1977, pp. 387–420.
doi: 10.1007/BF01228609

[4] Wyatt, S. P., *Dynamics of Satellites / Dynamique des Satellites: Symposium Paris, May 28–30, 1962 / Symposium Paris, 28–30 Mai 1962*, chap. The effect of terrestrial radiation pressure on satellite orbits,

Springer Berlin Heidelberg, Berlin, Heidelberg, 1963, pp. 180–196.
doi: 10.1007/978-3-642-48130-7_16

[5] Stephens, G. L., Campbell, G. G., , and Haar, T. H. Y., "Earth Radiation Budgets," *Journal of Geophysical Research*, Vol. 86, No. C10, 1981, pp. 9739–9760.
doi: 10.1029/JC086iC10p09739

[6] Rubincam, D. P. and Weiss, N. R., "Earth albedo and the orbit of Lageos," *Celestial mechanics*, Vol. 38, No. 3, 1985, pp. 233–296.
doi: 10.1007/BF01231110

[7] Rubincam, D. P., "Lageos Orbit Decay Due to Infrared Radiation From Earth," Tech. Rep. NASA Technical Memorandum 87804, NASA Goddard Space Flight Center, Greenbelt, Maryland, January 1987.

[8] Harris, A. W., "A Thermal Model for Near-Earth Asteroids," *Icarus*, Vol. 131, No. 2, 1998, pp. 291 – 301.
doi: 10.1006/icar.1997.5865

[9] Lebofsky, L. A., Sykes, M. V., Tedesco, E. F., Veeder, G. J., Matson, D. L., Brown, R. H., Gradie, J. C., Feierberg, M. A., and Rudy, R. J., "A refined "standard"İthermal model for asteroids based on observations of 1 Ceres and 2 Pallas," *Icarus*, Vol. 68, No. 2, 1986, pp. 239 – 251.
doi: 10.1016/0019-1035(86)90021-7

[10] Spencer, J. R., Lebofsky, L. A., and Sykes, M. V., "Systematic biases in radiometric diameter determinations," *Icarus*, Vol. 78, No. 2, 1989, pp. 337 – 354.
doi: 10.1016/0019-1035(89)90182-6

[11] Scheeres, D., "The dynamical evolution of uniformly rotating asteroids subject to YORP," *Icarus*, Vol. 188, No. 2, 2007, pp. 430 – 450.
doi: 10.1016/j.icarus.2006.12.015

[12] Montenbruck, O. and Gill, E., "Force Model," *Satellite Orbits: Models, Methods, and Applications*, 1st ed., Physics and astronomy online library, Springer Berlin Heidelberg, 2000, pp. 107–108.

[13] McInnes, C., "Solar Radiation Pressure," *Solar Sailing: Technology, Dynamics and Mission Applications*, Springer Praxis Books, Springer London, 2013, pp. 35–36.

[14] Müller, M., *Surface Properties of Asteroids from Mid-Infrared Observations and Thermophysical Modeling*, Ph.D. thesis, Freien Universität, Department of Earth Sciences, Berlin, 2007.

[15] Mohr, P. J., Newell, D. B., and Taylor, B. N., "CODATA recommended values of the fundamental physical constants: 2014," *arXiv:1507.07956*.

doi: 10.1103/RevModPhys.88.035009

[16] Jones, T. J. and Morrison, D., "Recalibration of the photometric/radiometric method of determining asteroid sizes," *Astronomical Journal*, Vol. 79, 1974, pp. 892 – 895.
doi: 10.1086/111626

[17] Mainzer, A., Usui, F., and Trilling, D. E., "Space-Based Thermal Infrared Studies of Asteroids," *Asteroids IV*, University of Arizona Press, Tucson, AZ, 2015, pp. 89–106.

[18] Lebofsky, L. A. and Spencer, J. R., "Radiometry and thermal modeling of asteroids," *Asteroids II*, University of Arizona Press, Tucson, AZ, 1989, pp. 128Ű–147.

[19] Delbo, M., Mueller, M., Emery, J. P., Rozitis, B., and Capria, M. T., "Asteroid Thermophysical Modeling,", *Asteroids IV*, University of Arizona Press, Tucson, AZ, 2015, pp. 107–128.

[20] Rozitis, B. and Green, S. F., "The influence of rough surface thermal-infrared beaming on the Yarkovsky and YORP effects," *Monthly Notices of the Royal Astronomical Society*, Vol. 423, No. 1, 2012, pp. 367–388.
doi: 10.1111/j.1365-2966.2012.20882.x

[21] Bottke, Jr., W. F., Vokrouhlický, D., Rubincam, D. P., and Broz, M., "The Effect of Yarkovsky Thermal Forces on the Dynamical Evolution of Asteroids and Meteoroids," *Asteroids III*, University of Arizona Press, Tucson, AZ, 2002, pp. 395–408.

[22] Paddack, S. J., "Rotational bursting of small celestial bodies: Effects of radiation pressure," *Journal of Geophysical Research*, Vol. 74, No. 17, 1969, pp. 4379 – 4381.
doi: 10.1029/JB074i017p04379

[23] McMahon, J. W. and Scheeres, D. J., "New Solar Radiation Pressure Force Model for Navigation," *Journal of Guidance, Control, and Dynamics*, Vol. 33, No. 5, 2010, pp. 1418 – 1428.
doi: 10.2514/1.48434

[24] McMahon, J. W. and Scheeres, D. J., "Improving Orbit Determination with Low-order Fourier Solar Radiation Pressure Models," *Proceedings of the AAS/AIAA Astrodynamics Conference* Hilton Head, SC, Aug. 11-15, 2013, pp. 1093–1112.

[25] Albuja, A. and Scheeres, D. J., "Defunct Satellites, Rotation Rates and the YORP Effect," *Proceedings of the Advanced Maui Optical and Space Surveillance Technologies Conference*, Wailea, Hawaii, 2013, pp. 156–163.

[26] Albuja, A. and Scheeres, D., "Effects of Optical and Geometrical Properties on YORP Effect for Inactive Satellites," *Proceedings of the Advanced Maui Optical and Space Surveillance Technologies Conference*, Wailea, Hawaii, Sep. 2014, p. 34.

[27] Albuja, A., Scheeres, D. J., and McMahon, J. W., "Evolution of angular velocity for defunct satellites as a result of YORP: An initial study," *Advances in Space Research*, Vol. 56, No. 2, 2015, pp. 237–251. doi: 10.1016/j.asr.2015.04.013

[28] Hesar, S. G., *A Framework for Precise Orbit Determination of Small Body Orbiting Spacecraft*, Ph.D. thesis, University of Colorado, Boulder, Boulder, CO 80309, 2016.

[29] Berry, K., Sutter, B., May, A., Williams, K., Barbee, B. W., Beckman, M., and Williams, B., "OSIRIS-REx Touch-And-Go (TAG) Mission Design and Analysis," *Proceedings of the 36th Annual AAS Guidance and Control Conference*, Breckenridge, CO, Feb. 1–6, 2015, pp. 667–678.

[30] Chesley, S. R., Farnocchia, D., Nolan, M. C., Vokrouhlický, D., Chodas, P. W., Milani, A., Spoto, F., Rozitis, B., Benner, L. A., Bottke, W. F., Busch, M. W., Emery, J. P., Howell, E. S., Lauretta, D. S., Margot, J.-L., and Taylor, P. A., "Orbit and bulk density of the OSIRIS-REx target Asteroid (101955) Bennu," *Icarus*, Vol. 235, 2014, pp. 5 – 22.
doi: 10.1016/j.icarus.2014.02.020

[31] Tapley, B. D., Schutz, B. E., and Born, G. H., "Fundamentals of Orbit Determination," *Statistical Orbit Determination*, Elsevier Academic Press, Burlington, MA, USA, 2004, pp. 230–233.